




Structural and magnetic properties of the quantum magnet $\text{BaCuTe}_2\text{O}_6$

A. Samartzis ^{1,2,*}, S. Chillal ¹, A. T. M. N. Islam,¹ K. Siemensmeyer,¹ K. Prokes,¹ D. J. Voneshen,^{3,4}
A. Senyshyn,⁵ D. Khalyavin,³ and B. Lake ^{1,2,†}

¹*Helmholtz-Zentrum Berlin für Materialien und Energie GmbH, Hahn-Meitner Platz 1, D-14109 Berlin, Germany*

²*Institut für Festkörperphysik, Technische Universität Berlin, Hardenbergstraße 36, D-10623 Berlin, Germany*

³*ISIS Facility, STFC Rutherford Appleton Laboratory, Oxfordshire OX11 0QX, United Kingdom*

⁴*Department of Physics, Royal Holloway University of London, Egham TW20 0EX, United Kingdom*

⁵*Heinz Maier-Leibnitz Zentrum, Lichtenbergstraße 1, D-85747 Garching, Germany*



(Received 23 November 2020; revised 29 January 2021; accepted 18 February 2021; published 11 March 2021)

We investigate the structural and magnetic properties of the quantum magnet $\text{BaCuTe}_2\text{O}_6$. This compound is synthesized in powder and single crystal form for the first time. Synchrotron x-ray and neutron diffraction reveal a cubic crystal structure ($P4_132$) where the magnetic Cu^{2+} ions form a complex network. Heat capacity and static magnetic susceptibility measurements suggest the presence of antiferromagnetic interactions with a Curie-Weiss temperature of ≈ -33 K, while long-range magnetic order occurs at the much lower temperature of ≈ 6.3 K. The magnetic structure, solved using neutron diffraction, reveals antiferromagnetic order along chains parallel to the a , b , and c crystal axes. This is consistent with the magnetic excitations which resemble the multispinon continuum typical of the spin-1/2 Heisenberg antiferromagnetic chain. A consistent intrachain interaction value of ≈ 34 K is achieved from the various techniques. Finally the magnetic structure provides evidence that the chains are coupled together in a noncollinear arrangement by a much weaker antiferromagnetic, frustrated hyperkagome interaction.

DOI: [10.1103/PhysRevB.103.094417](https://doi.org/10.1103/PhysRevB.103.094417)

I. INTRODUCTION

Quantum magnets are interesting because of their unusual ground states and excitations. They have strong quantum fluctuations which suppress long-range magnetic order and conventional spin-wave excitations, giving rise to novel states [1,2]. Typically quantum magnets have low spin quantum number that enhances quantum fluctuations and low-dimensional or frustrated interactions between the magnetic ions that suppress static magnetism. The simplest example of a quantum magnet is the spin-1/2 antiferromagnetic chain where the magnetic ions are coupled in one dimension only by antiferromagnetic nearest neighbor interactions [3–5]. This system does not develop long-range magnetic order even down to the lowest temperatures, and its excitations are spinons which have fractional spin quantum number $S = 1/2$ rather than spin waves or magnons which have $S = 1$ [6]. In higher dimensions quantum fluctuations can still arise in the case of frustrated interactions between the magnetic ions such as due to triangular or tetrahedral motifs [7–10]. Famous examples are the kagome [two-dimensional (2D) network of corner-sharing triangles] and pyrochlore [three-dimensional (3D) network of corner-sharing tetrahedra] lattices [11,12]. In the case of extreme magnetic frustration a quantum spin liquid state may be realized where there is total suppression of static

magnetism and the spins are moving coherently even at zero temperature [12–14].

Recently a family of quantum magnets with chemical formula ACuTe_2O_6 ($A = \text{Sr}, \text{Pb}$) was reported [15–22]. These compounds have cubic space group $P4_132$ where the magnetic Cu^{2+} ions ($S = 1/2$) occupy the $12d$ Wyckoff site. On its own the first neighbor interaction between the Cu^{2+} ions couples them into isolated triangles, the second neighbor interaction couples them in a hyperkagome lattice (3D network of corner-sharing triangles), and the third neighbor interaction couples them into chains [15,16,18]. Despite the fact that Sr^{2+} and Pb^{2+} have very similar sizes, $\text{SrCuTe}_2\text{O}_6$ and $\text{PbCuTe}_2\text{O}_6$ have very different interaction strengths and thus magnetic properties. In $\text{SrCuTe}_2\text{O}_6$ the third neighbor interaction is dominant and antiferromagnetic giving rise to spin-1/2 Heisenberg antiferromagnetic chains (HAFC), while the weaker first neighbor interactions act to couple these chains together and induce long-range magnetic order at a finite but suppressed Néel temperature (compared to the Curie-Weiss temperature) [15,18,19,21]. In contrast, for $\text{PbCuTe}_2\text{O}_6$ the first and second neighbor interactions are strong, antiferromagnetic, and approximately equal to each other giving rise to a highly frustrated 3D network of corner-sharing triangles called the hyper-hyperkagome lattice (related to but distinctly different from the hyperkagome lattice), while the weaker third neighbor interactions act to reduce the degree of frustration [15,16]. No long-range magnetic order has been observed in powder samples of $\text{PbCuTe}_2\text{O}_6$ down to 20 mK, and the excitations form very broad diffusive spheres completely different from the sharp

*alexandros.samartzis@helmholtz-berlin.de

†bella.lake@helmholtz-berlin.de

dispersive spin waves of a conventional 3D magnet [17]. These results suggest that $\text{PbCuTe}_2\text{O}_6$ is potentially close to a quantum spin liquid state.

In this paper, we investigate another member of the ACuTe_2O_6 family, namely $\text{BaCuTe}_2\text{O}_6$. It should be mentioned that $\text{BaCuTe}_2\text{O}_6$ has never been reported in the literature and has not been previously synthesized as far as we are aware. The Ba^{2+} ion is larger than Sr^{2+} and Pb^{2+} , thus we can expect that the exchange interactions and the magnetic properties may be different from those of $\text{SrCuTe}_2\text{O}_6$ and $\text{PbCuTe}_2\text{O}_6$. Here we report powder synthesis and growth of single crystals. We then determine the crystal structure using neutron and x-ray diffraction and find that $\text{BaCuTe}_2\text{O}_6$ is isostructural to other members of the family with cubic space group $P4_132$. Next we investigate the magnetic properties using DC magnetic susceptibility and heat capacity which reveal the presence of a phase transition to long-range magnetic order. We then solve the magnetic structure using neutron diffraction and investigate the excitations using inelastic neutron scattering. Our proposed coupling scheme is compared to that of $\text{SrCuTe}_2\text{O}_6$ and $\text{PbCuTe}_2\text{O}_6$.

II. SYNTHESIS OF $\text{BaCuTe}_2\text{O}_6$

We have performed the first powder synthesis and single crystal growth of $\text{BaCuTe}_2\text{O}_6$. The polycrystalline sample was synthesized by solid-state reaction using high purity powders of BaCO_3 (99.997% Alfa Aesar), CuO (99.995% Alfa Aesar), and TeO_2 (99.9995% Alfa Aesar). The initial powders were mixed thoroughly in the 1:1:2 molar ratio and heated in a vacuum furnace twice for 12 hours at 650°C under a flowing argon atmosphere with intermediate grindings. In order to confirm the chemical composition of $\text{BaCuTe}_2\text{O}_6$, x-ray diffraction was performed at room temperature using a Bruker D8 machine which also revealed that the powder was of high quality.

The crystal growth was carried out using the stoichiometric powder described above. After the second firing the powder was pulverized, packed into a cylindrical rubber tube, and pressed hydrostatically up to 2000 bars in a cold-isostatic-pressure (CIP) machine. The pressed rod was sintered in flowing argon in a vacuum furnace for 12 hours at 650°C to form a dense cylindrical rod with diameter ≈ 7 mm and length ≈ 7 –8 cm. Crystal growth was performed in an optical floating-zone furnace (Crystal Systems Corp., FZ-T 10000-H-VI-VPO) equipped with four 150 W Tungsten Halide lamps under 0.2 MPa argon atmosphere at a growth rate of 1.0 mm/h. The single crystallinity of the as-grown crystal was checked by a backscattering x-ray (molybdenum tube) Laue diffractometer [see Fig. 1(a)] and the cross section was checked by polarized optical microscopy. A piece of the crystal was also ground and checked with x-ray powder diffraction (Bruker D8) and found to be phase pure. From several growths, we identified three single crystals which were used for the present study; crystal III which has a length of 15.8 mm, diameter 5.5 mm, and weight 2.884 g is shown in Fig. 1(b). The synthesis and characterization of $\text{BaCuTe}_2\text{O}_6$ took place at the Core Laboratory for Quantum Materials, Helmholtz Zentrum Berlin für Materialien und Energie, Germany.

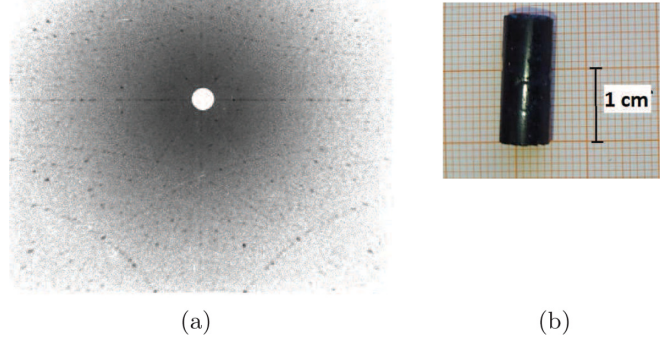


FIG. 1. (a) Laue diffraction pattern of a single crystal of $\text{BaCuTe}_2\text{O}_6$ with the x-ray beam parallel to the $[1\ 1\ 0]$ direction. From the figure it can be deduced that the illuminated surface of the crystal is single phased. (b) Crystal III which was used for the inelastic neutron scattering measurements due to its size and quality.

III. EXPERIMENTAL DETAILS

The crystal structure of the single crystals was studied via synchrotron x-ray diffraction at room temperature, performed using a wavelength of $0.493\ \text{\AA}$ on the Materials Science-beamline (MS-X04SA) [23] at the Paul Scherrer Institute (PSI) Switzerland. A small piece of single crystal was finely ground and mixed with diamond powder (ratio 1:3). The mixture was then placed in a thin capillary of 0.3 mm diameter which was spun continuously to avoid the effects of preferential orientation. The diffractometer measured a 2θ range of 110° with a resolution of 0.0036° .

Static dc-susceptibility (χ_{dc}) measurements were performed on a powder sample pressed into a thin pellet [$\sim 17.06(5)$ mg] over the temperature range 2–400 K under an applied magnetic field of 0.1 T. Heat capacity (C_p) measurements were performed on a pressed powder sample of $\sim 10.13(5)$ mg. Data were collected in the temperature range 2–100 K for zero applied magnetic field. These measurements were performed on a physical properties measurement system (PPMS, Quantum Design) and a magnetic properties measurement system (MPMS, SQUID VSM, Quantum Design) located at the Core Laboratory for Quantum Materials, Helmholtz Zentrum Berlin für Materialien und Energie, Germany.

Further structural characterization of $\text{BaCuTe}_2\text{O}_6$ was performed using the high resolution neutron powder diffractometer SPODI [24] at the Heinz Maier-Leibnitz Zentrum (MLZ) in Munich, Germany. A powder sample of mass 11.1(1) g was placed inside a copper can which was cooled in a ^3He cryostat. The diffraction patterns at $T = 0.5$ and 15 K were collected, using an incident wavelength of $1.548(2)\ \text{\AA}$ and a detector coverage of $2\theta = 151^\circ$ with a step size of 0.1° .

The magnetic structure of $\text{BaCuTe}_2\text{O}_6$ was refined from data [25] collected on a powder sample of mass 11.1(1) g measured by the high flux, high resolution neutron time-of-flight diffractometer (ToF) WISH [26], operated at Target Station 2 of the ISIS facility, Rutherford Appleton Laboratory, UK. A solid-methane moderator transmits incident neutrons between 1.5–15 \AA . Diffraction patterns were collected using 10 detec-

tor banks covering a total 2θ range of 160° and providing high resolution data over the whole wave-vector range. Data were collected between $T = 2$ and 8 K in 1 K steps. The FullProf Suite [27] was used to refine the diffraction data.

The spin dynamics of $\text{BaCuTe}_2\text{O}_6$ were studied by inelastic neutron scattering (INS). Data for both a powder and single crystal sample [28] were collected on the LET [29], cold neutron multichopper ToF spectrometer operating at Target Station 2 of the ISIS facility, Rutherford Appleton Laboratory, UK. The sample was cooled using an orange cryostat and data were measured at $T = 1.8$ K and 8 K. The spectrum of the powder sample [mass $10.1(4)$ g] was collected simultaneously using the five independent incident energies $E_i = 14.1, 4.88, 2.45, 1.47,$ and 0.978 meV with corresponding elastic energy resolutions, $\Delta E_i = 0.697, 0.144, 0.053, 0.025,$ and 0.014 meV for a total current of $240 \mu\text{A}$ and $310 \mu\text{A}$ at low and high temperatures, respectively. The single crystal sample consisted of three co-aligned crystals [of total mass $4.80(1)$ g] oriented with the $(1, -1, 0)$ crystallographic direction vertical. The crystals were wrapped in Al foil and attached using Al wire to an Al sample holder. This sample was measured at $T = 1.8$ K and $T = 8$ K with incident energies, $E_i = 13.75, 7.6, 4.81, 3.32,$ and 2.43 meV and corresponding elastic energy resolutions, $\Delta E_i = 0.782, 0.333, 0.175, 0.105,$ and 0.068 meV. During the measurements the crystals were rotated over an angular range of 159° in steps of 0.5° or 1° for a current of $8 \mu\text{A}$ per step.

IV. RESULTS AND DISCUSSIONS

A. Crystal structure

$\text{BaCuTe}_2\text{O}_6$ has never been previously reported in the literature, therefore our first task was to determine its crystal structure. We refined both synchrotron powder x-ray diffraction at 300 K measured on a crushed single crystal and neutron diffraction collected from the powder sample on two different instruments at temperatures temperature from 0.5 K to 15 K. The cubic space group $P4_132$ which describes the related compounds $\text{SrCuTe}_2\text{O}_6$ and $\text{PbCuTe}_2\text{O}_6$ was found to account entirely for the crystal structure of $\text{BaCuTe}_2\text{O}_6$ at all temperatures. At room temperature the lattice parameter was $a = 12.8330(2)$ Å (see Table II), and the atomic coordinates are listed in Table I along with the thermal parameters B_{iso} . The lattice parameter decreases slightly with decreasing temperature but no significant change in the atomic positions are found at low temperatures. Details of this analysis along with selected fitted diffraction patterns are given in Appendix A.

The crystal structure of $\text{BaCuTe}_2\text{O}_6$ is presented in Fig. 2. The Cu^{2+} ions in $\text{BaCuTe}_2\text{O}_6$ are magnetic with spin $S = 1/2$ angular momentum, there are 12 Cu^{2+} ions in each unit cell occupying the $12d$ Wyckoff site. Magnetic exchange interactions (super superexchange interactions) are expected between neighboring Cu^{2+} ions. Using the crystallographic parameters from the refinement of the synchrotron x-ray data, up to three nearest neighbor Cu^{2+} - Cu^{2+} bonds with successively increasing bond lengths are identified. The first nearest neighbor interaction, J_1 [bond distance $d_1 = 4.73(8)$ Å], couples the Cu^{2+} ions into isolated equilateral triangles. The second nearest neighbor interaction, J_2 [bond distance $d_2 = 5.65(8)$ Å], forms a network of corner-sharing equilateral triangles known as the hyperkagome lattice. Finally the

TABLE I. Atomic coordinates along with the thermal parameters B_{iso} from the Rietveld refinement within the $P4_132$ space group of the x-ray synchrotron pattern at room temperature of the crushed single crystal (top section) and the SPODI neutron scattering pattern of the powder sample prepared by solid state reaction at 15 K (bottom section).

Synchrotron x ray, crushed single crystal, 300 K					
Atom	Mult.	x	y	z	B_{iso}
Te	24e	0.3368(1)	0.9170(1)	0.0641(1)	1.14(1)
Ba1	8c	0.0586(1)	0.0586(1)	0.0586(1)	1.18(3)
Ba2	4b	0.3750	0.6250	0.1250	1.11(4)
Cu	12d	0.4741(1)	0.8750	0.2758(1)	1.18(5)
O1	24e	0.5794(6)	0.9231(6)	0.3697(6)	1.42(18)
O2	24e	0.2658(5)	0.8121(5)	0.9923(6)	1.05(18)
O3	24e	0.2227(6)	0.9743(7)	0.1342(7)	2.66(21)
Neutron, powder by solid state reaction, 15 K					
Atom	Mult.	x	y	z	B_{iso}
Te	24e	0.3371(3)	0.9180(3)	0.0640(3)	0.98(9)
Ba1	8c	0.0563(3)	0.0563(3)	0.0563(3)	0.36(19)
Ba2	4b	0.3750	0.6250	0.1250	0.96(24)
Cu	12d	0.4738(2)	0.8750	0.2761(2)	0.80(10)
O1	24e	0.5763(3)	0.9242(3)	0.3737(3)	1.02(10)
O2	24e	0.2662(2)	0.8115(5)	0.9900(3)	1.42(10)
O3	24e	0.2267(3)	0.9739(3)	0.1372(3)	1.39(9)

third neighbor interaction, J_3 [bond distance $d_3 = 6.48(0)$ Å], connects the Cu^{2+} ions into uniform chains along the a , b , and c crystallographic directions. These interactions are presented individually in Fig. 3. It should be mentioned that each Cu^{2+} ion is equivalent (single Wyckoff site $12d$) and participates in one J_1 triangle, two J_2 triangles, and one J_3 chain. In the case of antiferromagnetic J_1 and/or J_2 , geometrical magnetic frustration can be expected. The same set of interactions is found in the isostructural compounds $\text{PbCuTe}_2\text{O}_6$ and $\text{SrCuTe}_2\text{O}_6$ [16,20].

TABLE II. Crystallographic parameters of $\text{BaCuTe}_2\text{O}_6$ single crystal and powder samples obtained from the refinement of the synchrotron x-ray and neutron diffraction patterns at several temperatures. The lattice parameter a and refinement quality parameter R_{Bragg} are listed. The data were refined with the cubic space group $P4_132$ (#213) which accounts entirely for the crystal structure at all temperatures. The refinement of the WISH powder data includes two patterns from Banks 1 and 10 and Banks 2 and 9. The data at 2 K include a magnetic phase in the refinement.

T (K)	a (Å)	R_{Bragg} (%)
Synchrotron x rays, crushed single crystal		
300	12.8330(2)	9.87
Neutrons @ SPODI, powder from solid state reaction		
15	12.8328(1)	3.0
0.5	12.8218(8)	2.41
Neutrons @ WISH, powder from solid state reaction		
8	12.8287(2)	2.53
2	12.8277(8)	4.51

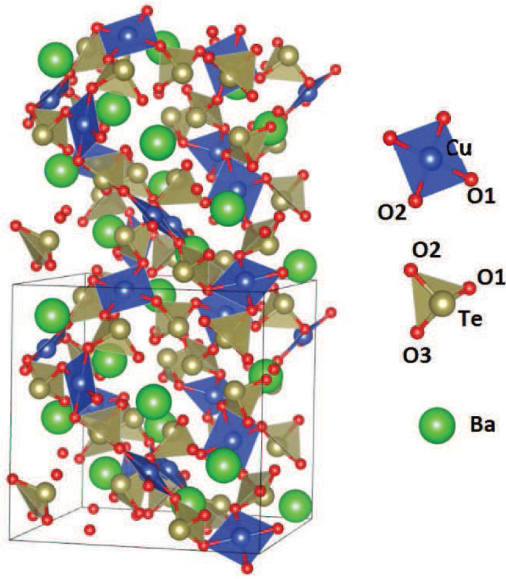


FIG. 2. Crystal structure of $\text{BaCuTe}_2\text{O}_6$ using the lattice parameters and atomic coordinates extracted from the analysis of the high-resolution synchrotron powder x-ray diffraction data at room temperature. The ions Ba^{2+} , Cu^{2+} , Te^{4+} , and O^{2-} are shown as green, blue, gold, and red spheres, respectively, and the coordination of Te^{4+} and Cu^{2+} by O^{2-} are shown by the polyhedra. The figure was prepared using the VESTA software [30].

B. Bulk physical properties

1. Static magnetic susceptibility

In order to investigate the magnetic properties of $\text{BaCuTe}_2\text{O}_6$, static magnetic susceptibility data χ_{dc} were collected on the powder sample in the temperature range $T = 2$ to 400 K for an applied magnetic field of $H = 0.1$ T. Figure 4(a) shows three distinctive temperature regions. The data at high temperature ($T > 50$ K) decreases smoothly with increasing temperature suggesting a paramagnetic state, while a broad maximum at ~ 22 K reflects the presence of short-range spin correlations which are a characteristic feature of magnets with low-dimensional and/or frustrated interactions.

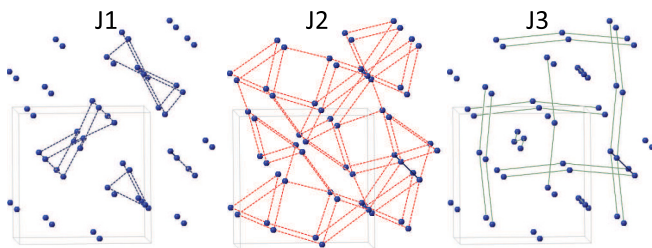


FIG. 3. The magnetic exchange interactions J_1 , J_2 , and J_3 between the Cu^{2+} ions in $\text{BaCuTe}_2\text{O}_6$ are presented from left to right. The first neighbor interactions, J_1 (black dashed lines), form isolated Cu^{2+} triangles. The second neighbor interactions, J_2 (red dashed lines), lead to a 3D network of corner sharing triangles, known as the hyperkagome lattice. The third neighbor interactions J_3 (green lines) form chains along the a , b , and c axes. Only the Cu^{2+} ions are shown (blue spheres) and the light gray lines indicate the boundaries of one unit cell. The figure was prepared by the Crystal Maker software [31].

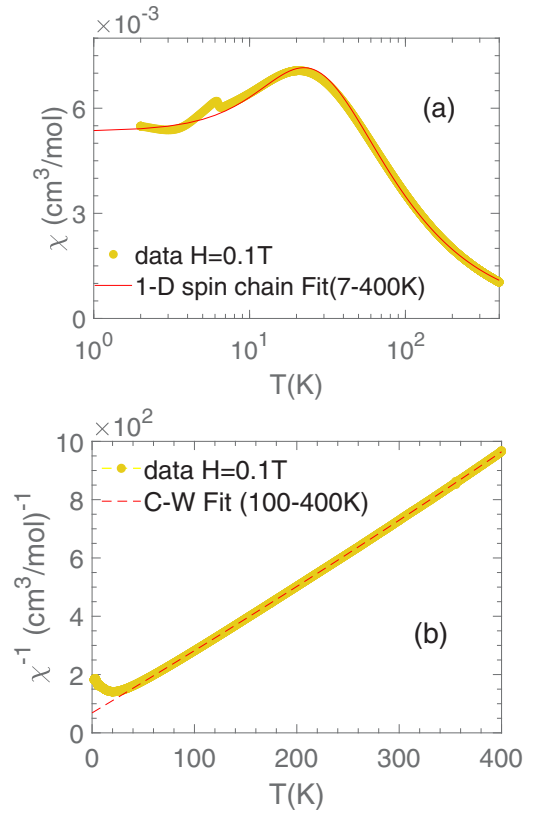


FIG. 4. (a) Temperature dependence of the static magnetic susceptibility χ_{dc} measured on a powder sample of $\text{BaCuTe}_2\text{O}_6$ in an applied magnetic field $H = 0.1$ T. The data in the range 7 K to 400 K were fitted by Eq. (1) which includes the $S=1/2$ HAFC model. (b) Inverse susceptibility as a function of temperature. The data in the range 100 K to 400 K were fitted to the Curie-Weiss Law.

The prominent sharp peak at $T_N = 6.31$ K reveals a magnetic phase transition to long-range magnetic order, while the susceptibility data increases with decreasing temperature below the transition suggesting a paramagnetic contribution from impurities and/or defects in the sample.

The data in the range 100 K to 400 K were fitted by the modified Curie-Weiss expression $\chi(T) = \chi_0 + C/(T + T_{\text{CW}})$ as shown by the red dotted line in Fig. 4(b) that presents the inverse susceptibility as a function of temperature. The constant term in the expression is associated with the susceptibility from core diamagnetism. T_{CW} is the Curie-Weiss temperature, and the parameter C is the Curie constant that is related to the effective moment via the relation $\mu_{\text{eff}} = \sqrt{3k_B C/N_A}$, where k_B and N_A are the Boltzmann constant and the Avogadro number, respectively. The best fit yields the values $\chi_0 = -0.0001(0)$ cm^3/mol and $C = 0.4806(3)$ $\text{cm}^3\text{K}/\text{mol}$ from which the effective moment $\mu_{\text{eff}} = 1.96(5)$ μ_B/Cu^{2+} was extracted. This value is slightly higher than the spin-only value of the free $S = 1/2$ Cu^{2+} ion ($\mu_{\text{eff}} = g\sqrt{S(S+1)} \mu_B \approx 1.73 \mu_B$, for $g = 2$). Finally the fitting suggests antiferromagnetic spin correlations with $T_{\text{CW}} = -32.8(1)$ K. In an unfrustrated magnet with 3D interactions the transition to long-range magnetic order occurs at a temperature close to the Curie-Weiss temperature, however in $\text{BaCuTe}_2\text{O}_6$ $T_N = 6.31$ K is almost five times smaller than T_{CW} ; this indicates the suppression of static magnetic

order due to magnetic frustration and/or low-dimensional interactions.

In order to acquire insight into the broad maximum at $T \approx 22$ K, the susceptibility data were compared to a model for the spin-1/2 Heisenberg antiferromagnetic chain (HAFC). This model was selected because of the similarity of the susceptibility of $\text{BaCuTe}_2\text{O}_6$ with that of the isostructural compound $\text{SrCuTe}_2\text{O}_6$, where the $J3$ interaction is dominant and couples the Cu^{2+} ions into antiferromagnetic chains along the a , b , and c crystallographic directions. We used the expression [32]

$$\chi(T) = \chi_0 + \chi_{1D}(T), \quad (1)$$

where the $\chi_{1D}(T)$ term is an expression for the susceptibility of the spin-1/2 HAFC calculated by S. Eggert *et al.* [33]

$$\chi_{1D}(T) = g^2 \left(\frac{N_A \mu_B^2}{4k_B} \right) F \left(\frac{J3}{k_B T} \right) \frac{1}{T}, \quad (2)$$

where

$$F(x) = \frac{1 + 0.08516x + 0.23351x^2}{1 + 0.73382x + 0.13696x^2 + 0.53568x^3}. \quad (3)$$

The χ_{dc} data in Fig. 4(a) were fitted by Eq. (1) (red line) in the temperature range 7 to 400 K. The χ_{1D} term yields $g \approx 2.096 \pm 0.002$ and $J3/k_B = 34.40(4)$ K for the g -factor and intrachain interaction strength, respectively, while the constant term is $\chi_0 = 0.0001(0)$ cm³/mol. The effective moment, given by $\mu_{\text{eff}} = \sqrt{3k_B C_{1D}/N_A} = 1.82 \pm 0.01 \mu_B/\text{Cu}^{2+}$ where $C_{1D} = g^2(N_A \mu_B^2/4k_B)$, agrees with the value of the free $S = 1/2 \text{ Cu}^{2+}$ ion.

2. Heat capacity

The heat capacity C_p of $\text{BaCuTe}_2\text{O}_6$ was investigated to provide further information about the magnetic properties. Data were collected on a powder sample in zero applied magnetic field, over the temperature range 2 to 100 K. Figure 5(a) presents the results where a sharp λ anomaly appears at $T \approx 6$ K suggesting a second order phase transition in agreement with the peak observed in the dc-susceptibility measurement. At higher temperatures the heat capacity increases with temperature. The C_p of $\text{BaCuTe}_2\text{O}_6$ has two contributions, phononic and magnetic; the magnetic contribution is expected at temperatures below $T_{\text{CW}} \approx 36$ K while the phonons dominate at higher temperatures. To model the lattice contribution a linear combination of n Debye integrals was fitted to the data for $T > 40$ K [34] using the expression

$$C_{\text{ph}}(T) = 9R \sum_{i=1}^n c_i \left(\frac{T}{T_{Di}} \right)^3 \int_0^{T_{Di}/T} \frac{x^4 e^x}{(e^x - 1)^2} dx, \quad (4)$$

where R is the universal gas constant and c_i is the i th coefficient with Debye temperature T_{Di} . The best fit was achieved for $n = 3$ as shown by the green line in Fig. 5(a), and the fitted parameters are given in the figure caption.

The pure magnetic C_{mag} contribution is shown by the black line and was obtained by subtracting the C_{ph} part from the data. Figure 5(b) presents C_{mag}/T as a function of T (yellow points, left-hand y axis) focusing on the low temperature region where the broad maximum at $T_m = 10.63(4)$ K is associated with short-range spin correlations while the sharp λ anomaly at $T_N = 6.32$ K indicates the transition to long-range magnetic order. The inset shows the region around T_N in

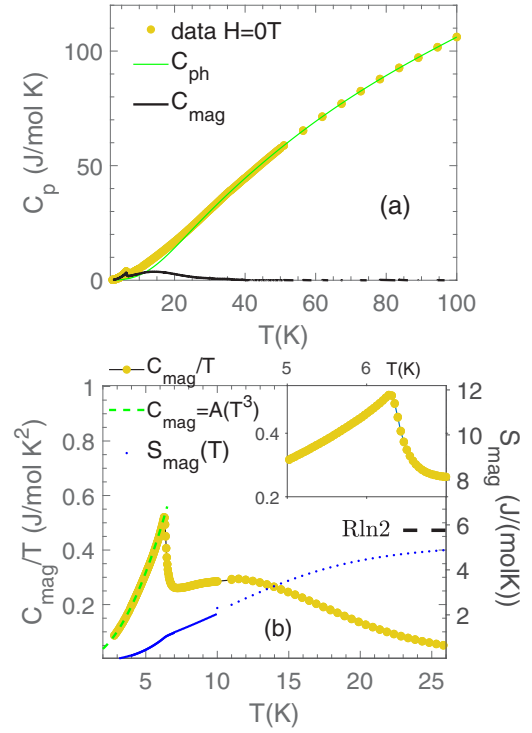


FIG. 5. (a) Heat capacity data collected as a function of temperature from a powder sample of $\text{BaCuTe}_2\text{O}_6$ in zero applied magnetic field. The data were fitted with a linear combination of three Debye terms above $T = 40$ K to model the lattice heat capacity (solid green line). The phononic parameters obtained from fitting Eq. (4) to the data are: $c_1 = 2.2(2)$ with $T_{Di} = 128(5)$, $c_2 = 2.96(6)$ with $T_{Di} = 333(15)$, and $c_3 = 37(3)$ with $T_{Di} = 1905(2)$. The magnetic heat capacity C_{mag} was obtained by subtracting the phononic contribution from the data (solid black line). (b) The low temperature C_{mag}/T is given by the yellow symbols (left-hand y axis) as a function of temperature and reveals a λ anomaly at $T_N = 6.32$ K. The green dashed line is a fit of C_{mag} below T_N , by the power law $C_{\text{mag}} = A(T^3)$. The temperature dependence of the magnetic entropy is given by the black dots (right-hand y axis).

detail and reveals a single transition in contrast to $\text{SrCuTe}_2\text{O}_6$ which has two distinct transitions. In order to estimate the exchange interaction $J3$ from the heat capacity data, we use the relation for a spin-1/2 Heisenberg antiferromagnetic chain [32], $J3/k_B = T_m/0.3071$, which yields $J3/k_B = 34.6(1)$ K confirming the result from the χ_{dc} measurement. Finally, the heat capacity below the transition follows a T^3 power law (shown by the green dashed line), which suggests the presence of a three-dimensional spin-wave dispersion at lowest energies and temperatures.

The magnetic entropy S_{mag} was calculated from the heat capacity and is plotted as a function of temperature in Fig. 5(b) (blue points, right-hand y axis). It increases with temperature reaching a value of $4.87 \text{ Jmol}^{-1} \text{ K}^{-1}$ at ~ 25 K above which it starts to approach the maximum value of $S_{\text{mag}} = R \ln 2 = 5.76 \text{ Jmol}^{-1} \text{ K}^{-1}$ expected for a spin-1/2 magnet. It should be noted that over the temperature range from 2 K to just above the transition at 7 K, only 21.2% of the full entropy is recovered; this is a feature typical of low-dimensional and/or frustrated magnets.

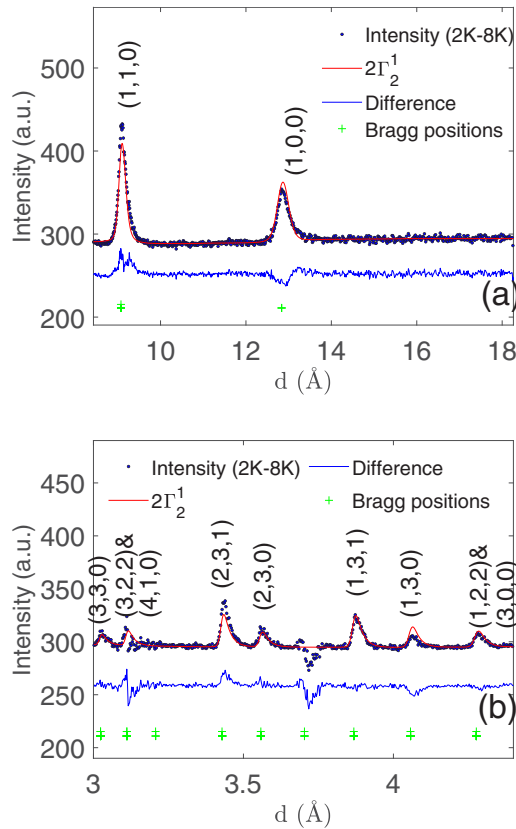


FIG. 6. Rietveld refinement of the magnetic diffraction pattern collected on (a) detector banks 1 and 10 showing the high d -spacing peaks, and (b) detector banks 2 and 9 showing the low d -spacing peaks, of the WISH diffractometer for a powder sample of $\text{BaCuTe}_2\text{O}_6$. The black circles give the result of subtracting the 8 K dataset from the 2 K dataset, the red line gives the refined fit of the data assuming the IR $2 \times \Gamma_2^1$ ($\chi^2 = 3.1$) while the blue line gives the difference between theory and experiment.

C. Magnetic structure

We now investigate the nature of the magnetic order occurring below T_N in $\text{BaCuTe}_2\text{O}_6$. The neutron diffraction data for the magnetic structure determination were collected on the WISH diffractometer which is an effective instrument for magnets with small ordered moments [26]. The difference pattern (the dataset at 2 K after subtraction of the 8 K dataset) is presented in Fig. 6 over selected d -space regions, and a list of the peaks that appear after this subtraction is presented in Table III (the difference patterns for the other detector banks are given in Appendix B). The Bragg peak at $d = 12.83 \text{ \AA}$ corresponds to the forbidden nuclear reflection (1,0,0) and is

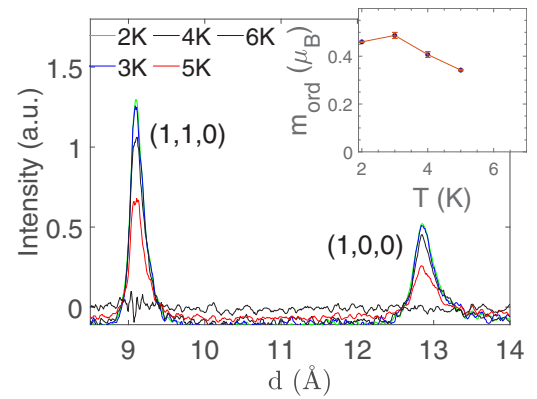


FIG. 7. Temperature dependence of the magnetic Bragg peaks obtained by subtracting the neutron diffraction pattern measured at 8 K from the $T = 2, 3, 4, 5,$ and 6 K neutron diffraction patterns. The datasets were collected from detector banks 1 and 10 of WISH. In the inset the fitted ordered moment m_{ord} is presented as a function of the temperature. The values were found after refining the data with the $2 \times \Gamma_2^1$ IR.

a clear indication of the magnetically ordered state at 2 K. All peaks can be indexed by the magnetic ordering vector, $k = (0, 0, 0)$, suggesting a commensurate magnetic structure.

Figure 7 presents the (1,0,0) and (1,1,0) [$d_{(110)} = 9.07 \text{ \AA}$] magnetic reflections at several different temperatures from 2 K to 6 K (after subtraction of the 8 K dataset). The intensity decreases with increasing temperature and disappears at 6 K suggesting that $\text{BaCuTe}_2\text{O}_6$ enters a long range magnetically ordered state below 6 K in agreement with the heat capacity and susceptibility data. Within the temperature steps that were measured no indication of a second transition is found.

We employed the standard representation theory approach [35], assuming that the magnetic structure is transformed by a single irreducible representation of the paramagnetic space group $P4_132$. The corresponding basis vectors were calculated using the software BASIREPS within the FullProf Suite [27]. The magnetic representation of the Cu^{2+} ion (Wyckoff site 12d) can be reduced into the following five irreducible representations (IRs) of the $P4_132$ space group, associated with the $k = (0, 0, 0)$ propagation vector:

$$\Gamma_{\text{mag,Cu}} = 1 \times \Gamma_1^1 + 2 \times \Gamma_2^1 + 3 \times \Gamma_3^2 + 4 \times \Gamma_4^3 + 5 \times \Gamma_5^3. \quad (5)$$

Each of the terms corresponds to one of the irreducible representations ($t \times \Gamma_o^d$) where the coefficient t gives the number of times it occurs, the subscript o gives the order of the representation, and the superscript d gives the dimensionality. The possible magnetic ground states are obtained from the

TABLE III. Peaks that appear after the subtraction of the $T = 8 \text{ K}$ from the $T = 2 \text{ K}$ datasets measured on the WISH detector banks 1, 2, 9 and 10.

(h, k, l)	(1,0,0)	(1,1,0)	(1,1,1)	(0,1,2)	(1,1,2)	(1,2,2) or (3,0,0)
$d \text{ (\AA)}$	12.8328	9.07409	7.40896	5.73896	5.23784	4.27757
(h, k, l)	(0,1,3)	(1,1,3)	(0,2,3)	(1,2,3)	(0,3,3)	(4,1,0) or (3,2,2)
$d \text{ (\AA)}$	4.05806	3.86920	3.55915	3.42968	3.02470	3.11099

combination of the basis vectors of each of the IRs, and the corresponding magnetic space groups were evaluated using the ISODISTORT software [36].

The candidate magnetic structures, whose magnetic space groups are consistent with the observed reflection conditions and are maximal isotropy subgroups of $P4_132$, were selected and systematically tested in the refinement procedure. As discussed in Appendix B, the $(H, H, 0)$ reflections (where H is an odd integer) are always present for $\text{BaCuTe}_2\text{O}_6$ while the (H, H, H) peaks are not observed except for $(1,1,1)$. This matches best with the cubic magnetic structure associated with the one-dimensional IR $2 \times \Gamma_2^1$ having the $P4_1'32'$ symmetry, for which $(H, H, 0)$ are allowed and (H, H, H) are forbidden. We believe the presence of the $(1,1,1)$ reflection is an artifact arising from the subtraction of the very strong nuclear contribution. This conclusion is supported by the absence of any magnetic contribution at the substantially weaker nuclear reflections $(2,2,2)$ and $(3,3,3)$ (see Appendix B).

The magnetic structure of $\text{BaCuTe}_2\text{O}_6$ was therefore refined using $2 \times \Gamma_2^1$ where the crystallographic parameters were fixed to the refined values found from the neutron diffraction measurement performed at 8 K. Figure 6 shows the best fit (red line) to the neutron diffraction data collected at 2 K (black circles) giving $\chi^2 = 3.1$. The difference between the fit and data is shown by the blue line and shows good agreement except for the $(1,1,1)$ peak. The ordered moment at 2 K was found to be $m_{\text{ord}} = 0.46 \mu_B/\text{Cu}^{2+}$. It is significantly suppressed compared to the value for the free Cu^{2+} ion of $1 \mu_B$. The suppression of the ordered moment is attributed to the presence of low-dimensional and/or frustrated antiferromagnetic interactions which give rise to strong spin fluctuations.

The $2 \times \Gamma_2^1$ IR found for $\text{BaCuTe}_2\text{O}_6$ contrasts with the $1 \times \Gamma_1^1$ IR, recently found for the isostructural compound $\text{SrCuTe}_2\text{O}_6$ [15,21], where the latter IR forbids both the $(H, H, 0)$ and (H, H, H) reflections. We therefore also refined the diffraction pattern of $\text{BaCuTe}_2\text{O}_6$ using the $1 \times \Gamma_1^1$ IR which gave the much worse goodness-of-fit of $\chi^2 = 8.5$. As shown in Appendix C, $1 \times \Gamma_1^1$ fails to reproduce the intensity at the $(1,1,0)$ peak and generally provides a much poorer fit over all d -spacing ranges than $2 \times \Gamma_2^1$. Hence, contrary to the findings for $\text{SrCuTe}_2\text{O}_6$, $2 \times \Gamma_2^1$ is the correct IR for $\text{BaCuTe}_2\text{O}_6$. The difference in the magnetic structure of these two compounds may be attributed to the difference in the ionic sizes of Ba^{2+} and Sr^{2+} , with the ionic radius of Ba^{2+} being 14% larger than that of Sr^{2+} , which could alter the bond distances and angles and hence the strength of the magnetic interactions.

We now discuss the higher order IRs, $3 \times \Gamma_3^2$, $4 \times \Gamma_4^3$, and $5 \times \Gamma_5^3$. The maximal magnetic subgroups associated with these IRs are inconsistent with the magnetic reflections of $\text{BaCuTe}_2\text{O}_6$. $3 \times \Gamma_3^2$ and $4 \times \Gamma_4^3$ have a systematic absence of the $(2n,0,0)$, $(0,2n+1,0)$, and $(0,0,2n+1)$ magnetic peaks (where n is an integer), thus we would expect to see $(2,0,0)$ in our powder measurement. Similarly $5 \times \Gamma_5^3$ is not compatible since it predicts the systematic absence of the $(H, H, 0)$ peaks whereas both $(1,1,0)$ and $(3,3,0)$ are present. We did not consider the candidate magnetic structures whose magnetic space groups are not maximal isotropy subgroups of $P4_132$. These magnetic structures require strongly first or

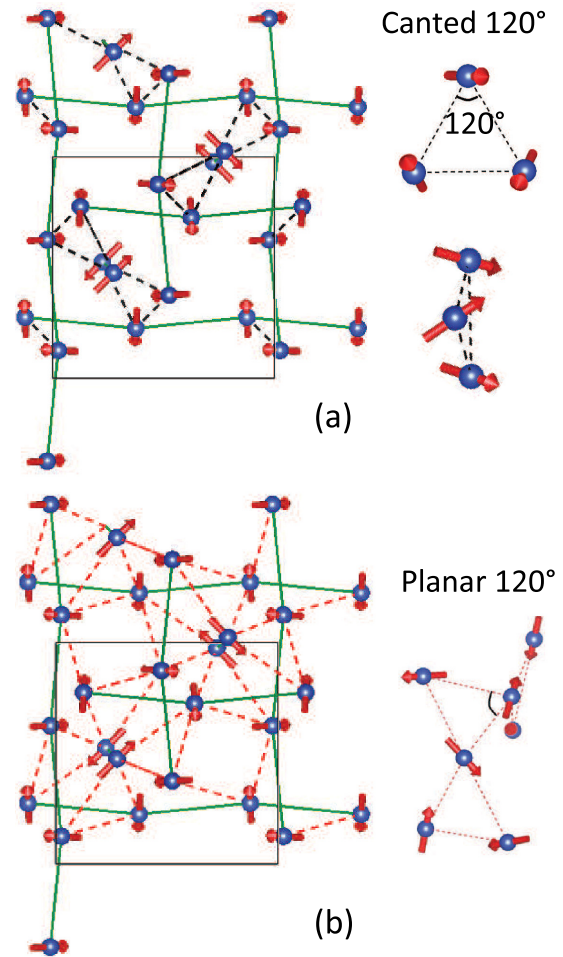


FIG. 8. Visualization of the magnetic structure of $\text{BaCuTe}_2\text{O}_6$ found by fitting the diffraction patterns measured at 2 K by the $2 \times \Gamma_2^1$ IR. Only the Cu^{2+} ions are shown represented by the blue spheres, while the red arrows indicate the directions of the ordered spin moments. (a) includes the first $J1$ (dotted black lines), and third $J3$ (solid green lines), nearest neighbor interactions while (b) includes the second $J2$ (dotted red line), and third $J3$ (solid green lines) nearest neighbor interactions. To the right of panel (a) [(b)], the triangles formed by $J1$ [$J2$] are presented. This figure was produced using the VESTA software [30].

der phase transitions and therefore are unlikely to occur in $\text{BaCuTe}_2\text{O}_6$.

The magnetic structure of $\text{BaCuTe}_2\text{O}_6$ is depicted in Fig. 8 where only the Cu^{2+} ions are shown (blue spheres) and the red arrows indicate the directions of their ordered spin moments. The magnetic interactions have also been included and by inspecting the relative alignment of the spins connected by these bonds, information about the size and sign of these interactions can be deduced. Figure 8(a) includes the first $J1$, and third $J3$, nearest neighbor interactions, represented by the dotted black and solid green lines, respectively. It is immediately apparent that the spins of the Cu^{2+} ions connected by $J3$ form antiferromagnetic chains, clearly identifying this interaction as antiferromagnetic. An isolated triangle formed by $J1$ is also presented separately on the right in planar and side views. The spins are noncollinear and have a strongly

canted structure. Their components in the plane of the triangle have a 120° arrangement typical of an antiferromagnetic interaction, while in contrast their components perpendicular to the plane are ferromagnetically aligned. This suggests that J_1 is too weak to influence the magnetic structure, and it is unclear whether it is ferromagnetic or antiferromagnetic. Figure 8(b) includes the second J_2 (dotted red lines), and third J_3 (solid green lines), nearest neighbor interactions. Three of the corner-sharing triangles formed by J_2 are shown on the right. The spins form a 120° arrangement in the plane of every triangle with zero out-of-plane component showing that this interaction is antiferromagnetic and sufficiently strong to influence the magnetic order. Altogether the magnetic structure of $\text{BaCuTe}_2\text{O}_6$ reveals that J_2 and J_3 are antiferromagnetic while J_1 is very weak.

Assuming spin chains created by J_3 which are coupled together by J_2 , a rough estimate of the size of J_2 can be found from the ordered moment m_{ord} via the expression $m_{\text{ord}} = 1.0197\sqrt{(J_2/J_3)}$ [37]. Using $J_3 = 34$ K, we get $J_2 = 6.91$ K. Since this expression applies to unfrustrated interchain coupling, we anticipate that it provides only an approximate lower limit on the frustrated J_2 interchain coupling of $\text{BaCuTe}_2\text{O}_6$.

D. Magnetic excitations

We now investigate the magnetic excitations of $\text{BaCuTe}_2\text{O}_6$. Figure 9 presents inelastic neutron scattering (INS) measured on the LET time-of-flight (ToF) spectrometer for a powder sample above the Néel temperature at 8 K [Fig. 9(a)] and below T_N at 1.8 K [Fig. 9(b)]. At 8 K, distinctive diffuse scattering occurs for energies below ≈ 7 meV which is identified as magnetic because its intensity decreases with increasing wave-vector transfer $|Q|$ in accordance with the magnetic form factor. There are other much weaker bands at higher energies, e.g., at $9 \text{ meV} < E < 11 \text{ meV}$, which are identified as having phononic origin since their intensity increases with increasing $|Q|$. The magnetic signal is generally sharper below T_N at 1.8 K and an additional signal appears below $E = 1.5$ meV. Figure 9(c) presents a cut through the data along energy at 1.8 K and 8 K with wave vector integrated over the range $1.0 \text{ \AA}^{-1} < |Q| < 2.0 \text{ \AA}^{-1}$ which shows a clear sharpening and intensity increase of the excitations due to the ordering of the magnetic moments below T_N .

In order to learn more about the spin dynamics of $\text{BaCuTe}_2\text{O}_6$, further INS data were collected on the LET spectrometer from a single crystal sample. Figure 10 presents the spectrum collected for an incident energy of $E_i = 4.81$ meV, integrated over the narrow energy transfer range $1.8 \text{ meV} < E < 2.2 \text{ meV}$ and plotted in the $[H, H, L]$ reciprocal plane. The data in Fig. 10(a) were measured at $T = 1.8$ K and in Fig. 10(b) at $T = 8$ K. At 8 K a highly symmetric pattern is revealed with two sets of parallel diffuse scattering streaks which are perpendicular to each other. Streaks of scattering observed in constant-energy slices indicate dispersionless excitations along the streak direction and are typical features of low-dimensional magnetism where the excitations are dispersionless in certain crystallographic directions. In the case of a magnet with one-dimensional interactions, the spectrum

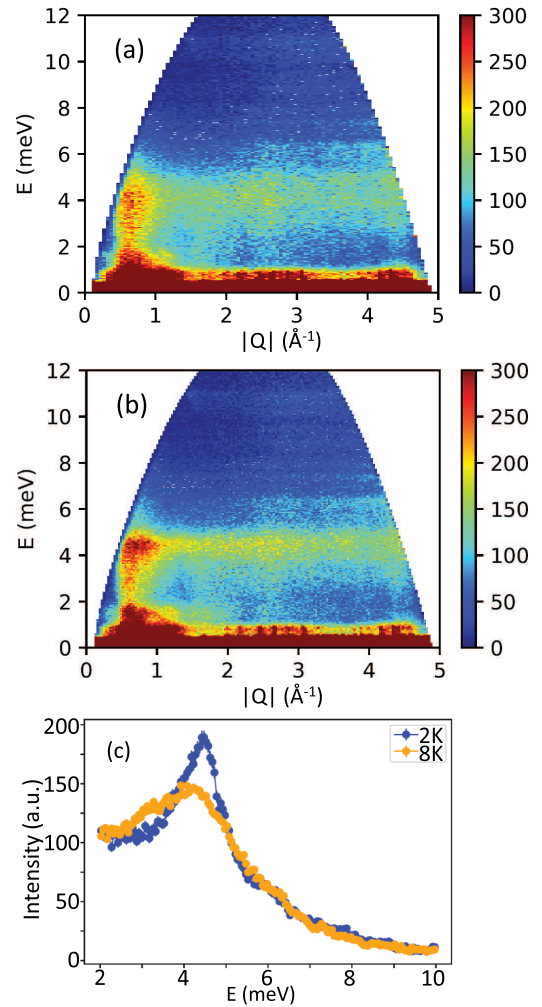


FIG. 9. Inelastic neutron scattering spectra as a function of energy and wave-vector transfer. The data were measured using the LET ToF spectrometer on a powder sample at $T = 8$ K (a) and $T = 1.8$ K (b) with an incident energy, $E_i = 14.10$ meV. No background has been subtracted from the data. (c) Energy cut through the data integrated over the wave-vector range $1.0 \text{ \AA}^{-1} < |Q| < 2.0 \text{ \AA}^{-1}$ and plotted as a function of energy. A broad maximum at ≈ 4 meV at $T = 8$ K (yellow symbols) becomes sharper at 4.5 meV in the ordered state at $T = 1.8$ K (blue symbols). With increasing energy, the signal drops gradually and seems unaffected by the temperature.

varies only along the chain direction and is dispersionless perpendicular to the chain.

In $\text{BaCuTe}_2\text{O}_6$ the only interaction which could give rise to the observed features is J_3 which couples the Cu^{2+} ions antiferromagnetically into mutually perpendicular chains along the a , b , and c directions. In contrast J_1 would produce a zero-dimensional magnetism while J_2 would result in three-dimensional magnetism. The first set of streaks which appears at integer values of L and runs parallel to the $[H, H, 0]$ direction arises from the spin chains along the c axis. The second set, which occurs at integer values of H and is parallel to $[0, 0, L]$, originate from the spin chains along the a and b axes. It is a characteristic feature that at odd values of H and L the streaks are systematically weaker than at even values. This scattering pattern sharpens below the transition at 1.8 K

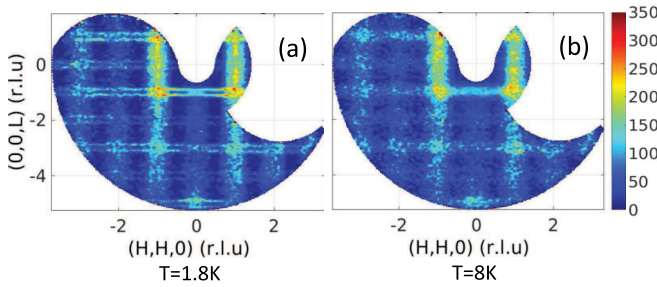


FIG. 10. Inelastic neutron scattering plotted as a function of wave-vector transfer in the $[H,H,L]$ plane at a constant energy transfer of 2.0 meV. The data was measured using the LET ToF spectrometer on a single crystal sample at $T = 1.8$ K (a) and $T = 8$ K (b) using an incident energy of $E_i = 4.81$ meV. The data was integrated over the energy transfer range $1.8 \text{ meV} < E < 2.2 \text{ meV}$ and over wave vector in the vertical out-of-plane direction by $[\pm 0.2, \mp 0.2, 0]$. No background subtraction has been performed and only a subtle smoothing is implemented.

[Fig. 10(a)] where the streaks split into closely spaced double streaks.

Energy slices as a function of wave vector parallel to the $[H, H, 0]$ and $[0, 0, L]$ directions can provide further insight into the spin dynamics. Figures 11(a)–11(d) present ToF INS spectra measured on LET with incident energy $E_i = 13.75$ meV, at $T = 1.8$ K [Figs. 11(a) and 11(c)] and $T = 8$ K [Figs. 11(b) and 11(d)]. The constant energy cuts along $[H, H, 0]$ [Figs. 11(a) and 11(b)] show dispersive features which are associated with the chains parallel to the a and b axes. Gapless, V-shaped excitations disperse up from the odd integer L and H reciprocal lattice points, while they are considerably weaker at even integer L and H values. The excitations are not sharp but form a continuum which broadens over wave vector with increasing energy transfer achieving strong intensity at $E \approx 5$ meV above which they weaken and then disappear for energies greater than 9 meV. The spectrum appears to become more intense and better defined below the Néel temperature than above. Figures 11(c) and 11(d) show the continuum along the $[0, 0, L]$ direction collected at 1.8 K [Fig. 11(c)] and at 8 K [Fig. 11(d)]. These features are associated with the chains parallel to the c axis and disperse up from the odd integer L reciprocal lattice points but are significantly weaker at even L .

The high energy excitations of $\text{BaCuTe}_2\text{O}_6$ resemble the spectrum of a spin-1/2 Heisenberg antiferromagnetic chain where they take the form of a broad multispinon continuum rather than conventional spin waves which would form sharp dispersive modes. Figure 11(e) shows the theoretical dynamical structure factor for the multispinon continuum according to the Bethe-Ansatz [38,39] which can be compared to the data. Note that because the structural unit cell contains two Cu^{2+} ions per chain, the multi-spinon continuum emerges from odd integer reciprocal lattice points rather than at half-integer values. The spinon continuum is contained between a lower and upper boundary given by the relations $E_L = (\pi/2)J_3 |\sin(\pi L)|$ and $E_U = \pi J_3 |\sin(\pi L/2)|$, respectively. The intensity is strongest at the lower boundary, and for half-integer values of L , a peak would be observed in

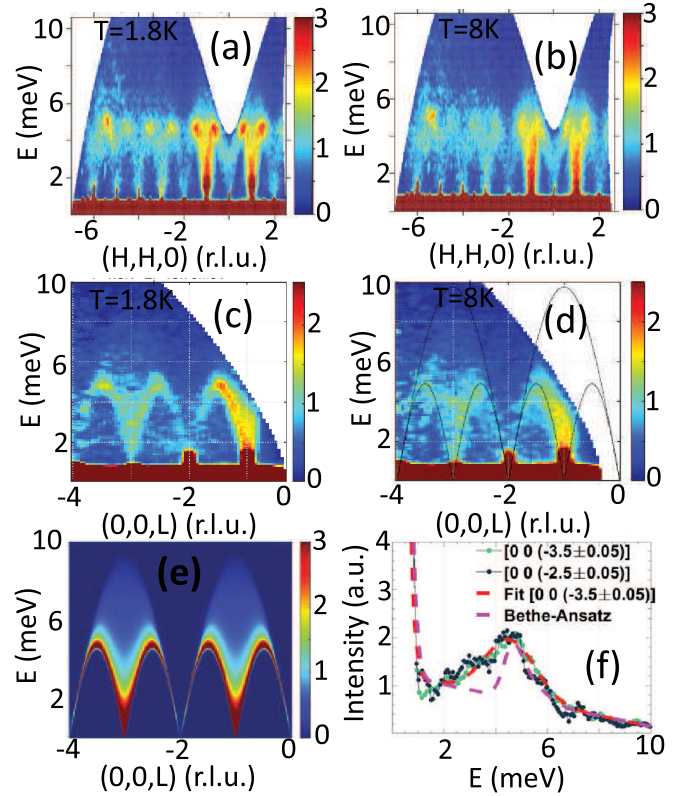


FIG. 11. (a)–(d) Inelastic neutron scattering measured on a single crystal sample plotted as a function of energy and wave-vector transfer without background subtraction. The data were collected on the LET ToF spectrometer using an incident neutron energy of $E_i = 13.75$ meV (energy resolution, 0.78 meV). (a) and (b) show the spectra along $[H, H, 0]$ collected at $T = 1.8$ K and $T = 8$ K, respectively. The data have been integrated by ± 0.2 r.l.u. over the $[0, 0, L]$ direction and by ± 0.5 r.l.u. over the $[K, -K, 0]$ vertical out-of-plane direction. (c) and (d) show the spectra along $[0, 0, L]$ collected at $T = 1.8$ K and $T = 8$ K, respectively. The data have been integrated by ± 0.2 r.l.u. over the $[H, H, 0]$ and $[K, -K, 0]$ directions. The ranges of integration were selected to achieve an adequate resolution and intensity. (e) Resolution corrected dynamical structure factor calculated via the algebraic Bethe-Ansatz for $J_3 = 2.90(6)$ meV. (f) Cuts along energy through the data collected with $E_i = 13.75$ meV and $T = 1.8$ K at $L = -2.5$ and -3.5 with integration over L of ± 0.05 , and over $[H, H, 0]$ and $[K, -K, 0]$ of ± 0.2 r.l.u. The red line gives the fit of a Gaussian to the $L = -3.5$ cut in order to extract the maximum of the lower boundary of the spinon continuum (red line). The magenta line gives the related cut through the theoretical dynamical structure factor calculated via the algebraic Bethe-Ansatz for $J_3 = 2.90(6)$ meV at $L = -3.5$. The fits include a sloping background and the elastic incoherent scattering peak.

a cut along energy marking the onset of the continuum at $E_L(\text{max}) = \pi J_3/2$; this can thus be used to extract the value of the intrachain interaction J_3 .

Figure 11(f) shows cuts through the 1.8 K dataset as a function of energy at $L = 2.5$ and 3.5 r.l.u. with a narrow integration range over L of ± 0.05 r.l.u. The data reveal a peak at $E_L(\text{max}) = 4.56(9)$ meV, as found by fitting a Gaussian on a sloping background to the data (red line). This gives

the size of the antiferromagnetic intrachain interaction as $J_3 = 2.90(6)$ meV or $33.7(7)$ K. The black line in Fig. 11(d) gives the boundaries of the two-spinon continuum calculated using the Bethe-Ansatz for $J_3 = 2.90(6)$ meV. The calculations are in good agreement with our data. Moreover, the J_3 value is found to be similar to the value extracted from dc susceptibility of $34.40(4)$ K and from heat capacity of $34.6(1)$ K. The consistency between the size of J_3 from different experimental measurements and the qualitative agreement of the experimental INS data with the Bethe-Ansatz theory, including the observation of continuum scattering, provide proof that the J_3 interaction is the dominant interaction and that BaCuTe₂O₆ is a good realization of the one-dimensional spin-1/2 Heisenberg antiferromagnet where the chains run parallel to the a , b , and c axes.

Finally, although J_1 and J_2 are clearly much weaker than J_3 , one or both of them must still be finite. As shown in Fig. 8, these interactions connect the chains together. In the absence of interchain coupling, a one-dimension magnet cannot develop long-range magnetic order according to the Mermin-Wagner theorem [40]. Since BaCuTe₂O₆ orders antiferromagnetically below $T_N = 6.3$ K the presence of J_1 and/or J_2 is confirmed.

V. SUMMARY AND CONCLUSIONS

In summary we have performed a detailed investigation of the quantum magnet BaCuTe₂O₆. We succeeded in making powders using the solid state reaction method and single crystals using the optical floating zone technique, and our characterizations suggest that our samples are pure and of high quality. Our synchrotron x-ray powder diffraction measurements reveal that BaCuTe₂O₆ crystallizes in the cubic space group $P4_132$ ($a = 12.83$ Å) and is isostructural to the other members of this family, SrCuTe₂O₆ and PbCuTe₂O₆. Neutron powder diffraction performed using a cryostat shows that this structure is stable down to $T = 0.5$ K. DC susceptibility measurements find a negative Curie-Weiss temperature $T_{CW} = -32.8(1)$ K suggesting predominantly antiferromagnetic spin interactions, while a transition to long-range antiferromagnetic order occurs at $T_N = 6.31$ K. The much lower value of T_N compared to T_{CW} as well as the broad maximum observed at ≈ 22 K reveal the presence of quantum fluctuations that suppress the onset of static magnetic order. Heat capacity measurements confirm the magnetic phase transition at $T_N = 6.32$ K and also show a broad maximum at ≈ 10.6 K.

Powder neutron diffraction reveals a commensurate magnetic structure with propagation vector $k = (0, 0, 0)$ and a drastically suppressed ordered moment of $0.46 \mu_B/\text{Cu}^{2+}$ at 2 K, compared to the Cu^{2+} moment of $1 \mu_B$ again confirming the presence of strong quantum fluctuations in the ground state. Inelastic neutron scattering reveals that these fluctuations are due to the dominant antiferromagnetic J_3 interaction which couples the spins into independent chains along the a , b , and c axes. The multispinon continuum, characteristic of the spin-1/2 HAFc, is observed along the chain directions giving an intrachain interaction value $J_3 = 33.7(7)$ K, while streaks of scattering are found perpendicular to the chains. The J_1 and/or J_2 interactions couple the chains together giving rise to the long-range magnetic order. Inspection of the magnetic

structure shows that the spins form a 120° magnetic order about the triangles coupled by the J_2 hyperkagome interaction suggesting that this interaction is antiferromagnetic. On the other hand the isolated triangles coupled by J_1 show a strongly canted 120° structure that fully satisfies neither an antiferromagnetic nor a ferromagnetic interaction revealing that J_1 is much weaker than J_2 .

Of the two isostructural compounds SrCuTe₂O₆ and PbCuTe₂O₆, BaCuTe₂O₆ appears to be most similar to SrCuTe₂O₆ where the chain interaction J_3 is dominant and antiferromagnetic and the ground state has long-range magnetic order. Their energy scales are also similar with $J_3 \approx 34$ K for BaCuTe₂O₆ and ≈ 50 K for SrCuTe₂O₆. Nevertheless these two compounds have different magnetic structures, SrCuTe₂O₆ orders in the Γ_1^1 IR with a 120° spin arrangement around the J_1 triangles suggesting that this interaction is antiferromagnetic and is responsible for coupling the chains together, while for BaCuTe₂O₆ which orders in the Γ_2^1 IR, J_2 is antiferromagnetic and primarily responsible for the interchain coupling. The differences between BaCuTe₂O₆ and SrCuTe₂O₆ are probably related to the larger ionic radius of Ba^{2+} compared to Sr^{2+} . In contrast PbCuTe₂O₆ is very different from both BaCuTe₂O₆ and SrCuTe₂O₆ even though Pb^{2+} and Sr^{2+} have the same ionic radius. In PbCuTe₂O₆ J_1 and J_2 are antiferromagnetic and of the same strength while J_3 is significantly weaker; this difference might be related to the lone pair of Pb^{2+} . The crystal structure of the ACuTe₂O₆ family is complex and the magnetic interactions include super-superexchange paths, thus subtle differences in bond distances and angles may cause significant changes in interaction strength.

To conclude, BaCuTe₂O₆ is a quantum magnet consisting of both frustrated and low-dimensional interactions that result in long-range magnetic order coexisting with strong quantum fluctuations. Future studies will focus on obtaining a better understanding of magnetic exchange paths from the low energy spin dynamics and *ab initio* calculations.

ACKNOWLEDGMENTS

We thank Jean-Sébastien Caux for his calculation of the dynamical structure factor of the spin-1/2 Heisenberg antiferromagnetic chain. B.L. acknowledges the support of DFG through project B06 of SFB 1143 (ID 247310070). The powder synthesis, crystal growth, and physical properties measurements took place at the Core Laboratory Quantum Materials, Helmholtz Zentrum Berlin für Materialien und Energie, Germany. We gratefully acknowledge the Science and Technology Facilities Council (STFC) for access to neutron beamtime at the LET and WISH ISIS facilities and also for the provision of sample preparation. We acknowledge Dr. Nicola P. M. Casati from Laboratory for Synchrotron Radiation-Condensed Matter, Paul Scherrer Institut (PSI) for the synchrotron x-ray powder diffraction measurements on the Materials Science beamline (MS-X04SA).

APPENDIX A: STRUCTURAL DETERMINATION

Figure 12(a) shows the room temperature high-resolution synchrotron x-ray diffraction pattern of BaCuTe₂O₆ measured

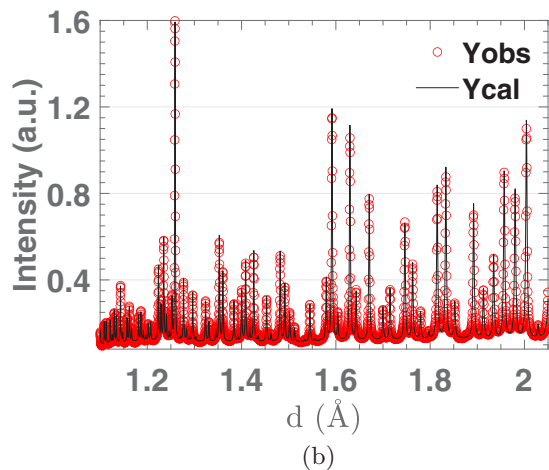
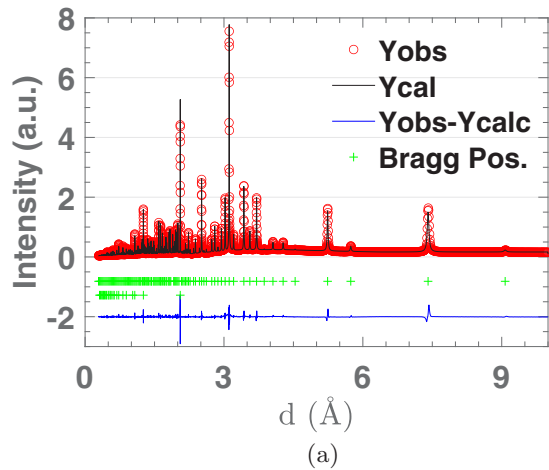


FIG. 12. (a) Structural Rietveld refinement (black line) of the synchrotron x-ray diffraction pattern (red circles) collected for a crushed single crystal of $\text{BaCuTe}_2\text{O}_6$ at room temperature along with the difference between the fit and data (blue line). The green crosses indicate the Bragg peak positions for the two included phases, $\text{BaCuTe}_2\text{O}_6$ (top row) and diamond powder (bottom row). The refinement confirms the cubic space group ($P4_132$) with lattice parameter $a = 12.8330(2)$ Å, achieved with $\chi^2 = 15.0$. (b) A small region of the diffraction pattern at low d spacing showing the goodness of the refinement.

on a crushed piece of single crystal. The diffraction pattern was refined within the cubic space group $P4_132$. The wavelength of the synchrotron x rays [$\lambda = 0.4930(4)$ Å] and the instrument profile parameters were determined by refining the x-ray diffraction profiles of standard Si 640d and LaB_6 powders, respectively, which were collected with the same instrumental settings. From the Rietveld refinement the lattice parameter was found to be $a = 12.8330(2)$ Å. The goodness of the refinement is confirmed further by Fig. 12(b) which presents an expanded view focusing on the low d -spacing range.

The neutron powder diffraction measurements were performed using the SPODI and WISH diffractometers. These measurements were performed on the powder sample of $\text{BaCuTe}_2\text{O}_6$ prepared by solid state reaction rather than the crushed single crystal. The sample was measured down to low

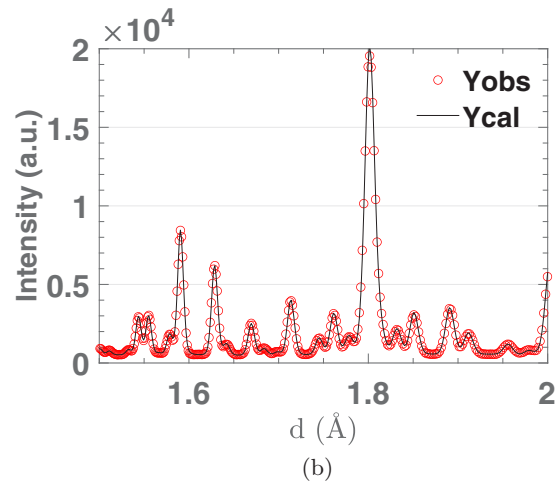
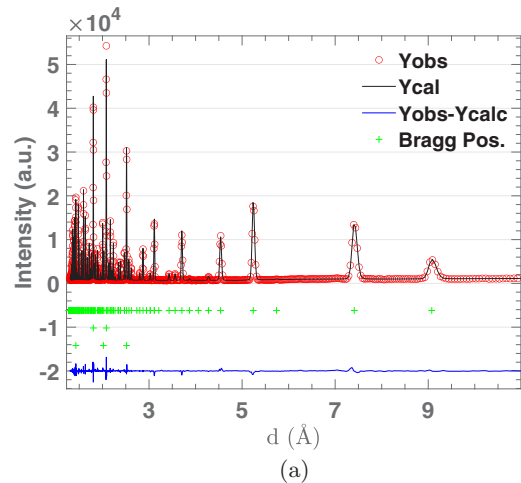


FIG. 13. (a) Rietveld refinement of the neutron powder diffraction pattern of the $\text{BaCuTe}_2\text{O}_6$ powder sample prepared by solid state reaction, collected at $T = 15$ K on the SPODI diffractometer. The red open circles refer to the experimental data, and the black and blue lines indicate the refined fit of the data and the difference between fit and experiment, respectively. The green crosses denote the Bragg peak positions for the three included phases, $\text{BaCuTe}_2\text{O}_6$, Cu container, and the Al cryostat. The refinement confirms the cubic space group $P4_132$ with lattice parameter $a = 12.8328(1)$ Å. (b) A small region of the diffraction pattern at low d spacing showing the goodness of the refinement.

temperatures so that any changes in crystal structure could be observed. All the data down to $T = 0.5$ K could be refined with the cubic space group $P4_132$, and no evidence for a structural phase transition was found. Figure 13(a) presents the powder diffraction pattern collected on SPODI at $T = 15$ K along with the Rietveld refinement; the accuracy of the refinement is highlighted by a selected low d -spacing range, presented in Fig. 13(b).

APPENDIX B: ALLOWED MAGNETIC PEAKS

Figure 14 compares the neutron powder diffraction patterns collected above and below T_N at $T = 8$ K and $T = 2$ K, respectively, for the various detector banks of the WISH diffractometer. The difference between the patterns (2 K

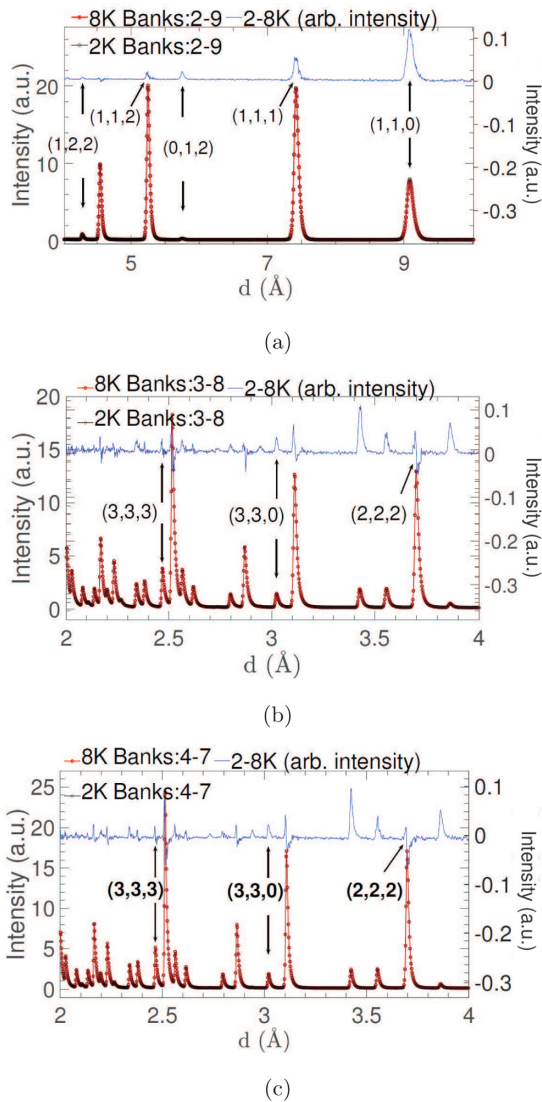


FIG. 14. (a) Neutron powder diffraction data collected above and below the magnetic phase transition at $T = 8$ K (red points) and 2 K (black points), respectively, on the WISH diffractometer plotted as a function of d spacing. The difference pattern (dataset at 2 K with the 8 K dataset subtracted) is also plotted as shown by the blue symbols (the y scale is shifted for clarity and shown on the right-hand side). The peaks are identified by their Miller indices. (a) shows the pattern at high d spacing collected from detector banks 2 and 9 while the lower d -spacing range is shown by (b) detector banks 3 and 8 and (c) detector banks 4 and 7.

dataset with 8 K dataset subtracted) is also presented in each case. The difference patterns show a series of peaks which are labeled by their Miller indices. Figure 14(a) shows the high d -spacing peaks (detector banks 2 and 9) and the difference pattern reveals the presence of (1,1,0), (1,1,1), (0,1,2), and (1,1,2). It should be mentioned, however, that the (1,1,0) and (1,1,1) nuclear peaks are among those with the highest intensity and their apparent increase in intensity at low temperatures could be unreliable resulting from the subtraction of two large numbers rather than the presence of additional magnetic intensity.

In order to establish a consistent set of rules governing the magnetic peaks allowed in $\text{BaCuTe}_2\text{O}_6$, the remaining WISH detector banks, which focus on the lower d spacings where the nuclear peaks that have weaker intensities were also considered. Because these nuclear peaks are weaker, we anticipate that the result of subtracting the high from the low temperature datasets will be more reliable. Figures 14(b) and 14(c) present the combined signal of detector banks 3 and 8 and banks 4 and 7, respectively. Both difference patterns clearly show the presence of the (3,3,0) reflection while the (2,2,2) and (3,3,3) reflections are absent. We conclude that the $(H, H, 0)$ reflections are allowed by the magnetic structure of $\text{BaCuTe}_2\text{O}_6$ but that the (H, H, H) reflections are absent, and therefore that the (1,1,1) peak observed in the difference pattern from detector banks 2 and 9 [Fig. 14(a)] is an artifact arising from the subtraction of the strong (1,1,1) nuclear reflection.

APPENDIX C: MAGNETIC REFINEMENT USING $1 \times \Gamma_1^1$

Since the magnetic structure of $\text{SrCuTe}_2\text{O}_6$ which is isostructural to $\text{BaCuTe}_2\text{O}_6$ orders within the $1 \times \Gamma_1^1$ IR

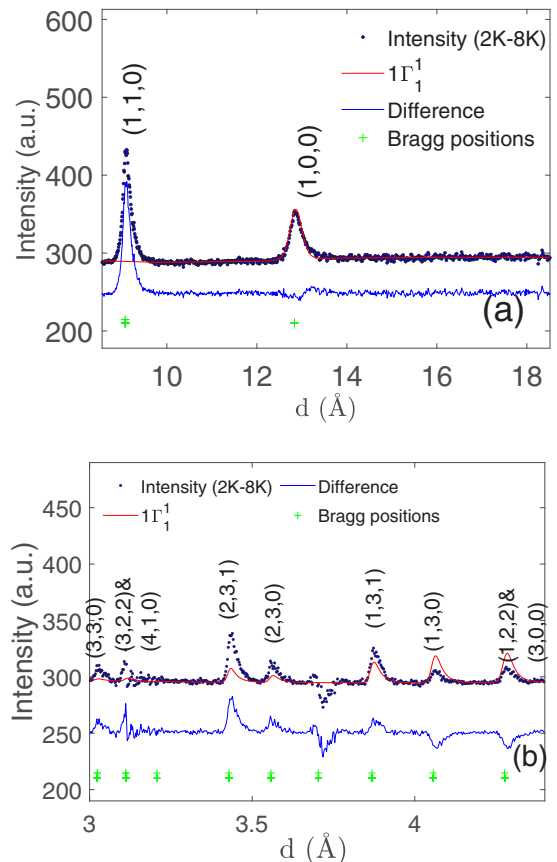


FIG. 15. Rietveld refinement of the magnetic diffraction pattern collected on (a) detector banks 1 and 10 showing the high d -spacing peaks and (b) detector banks 2 and 9 showing the low d -spacing peaks of the WISH diffractometer for a powder sample of $\text{BaCuTe}_2\text{O}_6$. The black circles give the result of subtracting the 8 K dataset from the 2 K dataset, the red line gives the refined fit of the data assuming the IR $1 \times \Gamma_1^1$ ($\chi^2 = 8.5$), while the blue line gives the difference between theory and experiment.

[15,21], this IR was used to refine $\text{BaCuTe}_2\text{O}_6$ for comparison with the $2 \times \Gamma_2^1$ IR refinement given in Fig. 6. Figures 15(a) and 15(b) present the Rietvelt refinement (red line) of the magnetic diffraction pattern (black circles) collected on detector banks 1 and 10 showing the high d -spacing peaks and de-

detector banks 2 and 9 showing the low d -spacing peaks, respectively. $1 \times \Gamma_1^1$ IR forbids both the (H,H,0) and (H,H,H) reflections, thus it fails to reproduce the intensity at the (1,1,0) peak and generally gives a much poorer fit over all d -spacing ranges with a χ^2 value of 8.5 compared to 3.1 for the $2 \times \Gamma_2^1$ IR.

-
- [1] L. Balents, *Nature (London)* **464**, 199 (2010).
- [2] C. Lacroix, P. Mendels, and F. Mila, *Introduction to Frustrated Magnetism: Materials, Experiments, Theory* (Springer, Berlin, 2013).
- [3] J. des Cloizeaux and J. J. Pearson, *Phys. Rev.* **128**, 2131 (1962).
- [4] B. Lake, D. A. Tennant, C. D. Frost, and S. E. Nagler, *Nat. Mater.* **4**, 329 (2005).
- [5] B. Lake, D. A. Tennant, J.-S. Caux, T. Barthel, U. Schollwöck, S. E. Nagler, and C. D. Frost, *Phys. Rev. Lett.* **111**, 137205 (2013).
- [6] M. Mourigal, M. Enderle, A. Klöpperpieper, J.-S. Caux, A. Stunault, and H. M. Rønnow, *Nat. Phys.* **9**, 435 (2013).
- [7] S. T. Bramwell and M. J. P. Gingras, *Science* **294**, 1495 (2001).
- [8] M. J. P. Gingras and P. A. McClarty, *Rep. Prog. Phys.* **77**, 056501 (2014).
- [9] C. Castelnovo, R. Moessner, and S. Sondhi, *Annu. Rev. Condens. Matter Phys.* **3**, 35 (2012).
- [10] J. S. Gardner, M. J. P. Gingras, and J. E. Greedan, *Rev. Mod. Phys.* **82**, 53 (2010).
- [11] J. G. Rau and M. J. P. Gingras, *Annu. Rev. Condens. Matter Phys.* **10**, 357 (2019).
- [12] Y. Zhou, K. Kanoda, and T.-K. Ng, *Rev. Mod. Phys.* **89**, 025003 (2017).
- [13] L. Savary and L. Balents, *Rep. Prog. Phys.* **80**, 016502 (2016).
- [14] T. Fennell, *Collection SFN* **13**, 04001 (2014).
- [15] S. Chillal, Y. Iqbal, H. O. Jeschke, J. A. Rodriguez-Rivera, R. Bewley, P. Manuel, D. Khalyavin, P. Steffens, R. Thomale, A. T. M. N. Islam, J. Reuther, and B. Lake, *Nat. Commun.* **11**, 2348 (2020).
- [16] B. Koteswararao, R. Kumar, P. Khuntia, S. Bhowal, S. K. Panda, M. R. Rahman, A. V. Mahajan, I. Dasgupta, M. Baenitz, K. H. Kim, and F. C. Chou, *Phys. Rev. B* **90**, 035141 (2014).
- [17] P. Khuntia, F. Bert, P. Mendels, B. Koteswararao, A. V. Mahajan, M. Baenitz, F. C. Chou, C. Baines, A. Amato, and Y. Furukawa, *Phys. Rev. Lett.* **116**, 107203 (2016).
- [18] N. Ahmed, A. A. Tsirlin, and R. Nath, *Phys. Rev. B* **91**, 214413 (2015).
- [19] B. Koteswararao, S. K. Panda, R. Kumar, K. Yoo, A. V. Mahajan, I. Dasgupta, B. H. Chen, K. H. Kim, and F. C. Chou, *J. Phys.: Condens. Matter* **27**, 426001 (2015).
- [20] B. Koteswararao, K. Yoo, F. Chou, and K. Kim, *APL Mater.* **4**, 036101 (2016).
- [21] P. Saeun, Y. Zhao, P. Piyawongwatthana, T. J. Sato, F. C. Chou, M. Avdeev, G. Gitgeatpong, and K. Matan, *Phys. Rev. B* **102**, 134407 (2020).
- [22] S. Chillal, A. T. M. N. Islam, H. Luetkens, E. Canévet, Y. Skourski, D. Khalyavin, and B. Lake, *Phys. Rev. B* **102**, 224424 (2020).
- [23] P. R. Willmott, D. Meister, S. J. Leake, M. Lange, A. Bergamaschi, M. Böge, M. Calvi, C. Cancellieri, N. Casati, A. Cervellino, Q. Chen, C. David, U. Flechsig, F. Gozzo, B. Henrich, S. Jäggi-Spielmann, B. Jakob, I. Kalichava, P. Karvinen, J. Krempasky, A. Lüdeke, R. Lüscher, S. Maag, C. Quitmann, M. L. Reinle-Schmitt, T. Schmidt, B. Schmitt, A. Streun, I. Vartiainen, M. Vitins, X. Wang, and R. Wulschleger, *J. Synchrotron Radiat.* **20**, 667 (2013).
- [24] M. Hoelzel, A. Senyshyn, N. Juenke, H. Boysen, W. Schmahl, and H. Fuess, *Nucl. Instrum. Methods Phys. Res., Sect. A* **667**, 32 (2012).
- [25] WISH, doi: [10.5286/ISIS.E.RB1620302](https://doi.org/10.5286/ISIS.E.RB1620302) (2018).
- [26] L. Chapon, P. Manuel, P. Radaelli, C. Benson, L. Perrott, S. Ansell, N. Rhodes, D. Raspino, D. Duxbury, E. Spill, and J. Norris, *Neutron News* **22**, 22 (2011).
- [27] J. Rodriguez-Carvajal, *Phys. B: Condens. Matter* **192**, 55 (1993).
- [28] LET, doi: [10.5286/ISIS.E.RB1710246](https://doi.org/10.5286/ISIS.E.RB1710246) (2017).
- [29] R. Bewley, J. Taylor, and S. Bennington, *Nucl. Instrum. Methods Phys. Res., Sect. A* **637**, 128 (2011).
- [30] K. Momma and F. Izumi, *J. Appl. Crystallogr.* **41**, 653 (2008).
- [31] D. C. Palmer, CrystalMaker (2014).
- [32] D. C. Johnston, R. K. Kremer, M. Troyer, X. Wang, A. Klümper, S. L. Bud'ko, A. F. Panchula, and P. C. Canfield, *Phys. Rev. B* **61**, 9558 (2000).
- [33] S. Eggert, I. Affleck, and M. Takahashi, *Phys. Rev. Lett.* **73**, 332 (1994).
- [34] C. Kittel, *Introduction to Solid State Physics*, 8th ed. (Wiley, 2004).
- [35] Y. Izumov, V. Naish, and R. Ozerov, *Neutron Diffraction of Magnetic Materials* (Springer US, 1991).
- [36] B. J. Campbell, H. T. Stokes, D. E. Tanner, and D. M. Hatch, *J. Appl. Crystallogr.* **39**, 607 (2006).
- [37] H. J. Schulz, *Phys. Rev. Lett.* **77**, 2790 (1996).
- [38] G. Müller, H. Thomas, H. Beck, and J. C. Bonner, *Phys. Rev. B* **24**, 1429 (1981).
- [39] J.-S. Caux and J. M. Maillet, *Phys. Rev. Lett.* **95**, 077201 (2005).
- [40] N. D. Mermin and H. Wagner, *Phys. Rev. Lett.* **17**, 1133 (1966).